Two-Fluid and Finite Larmor Radius Effects on Helicity Evolution in a Plasma Pinch

J. P. Sauppe[1, 2, a)] and C. R. Sovinec[1, 3, b)]
[1)] *Center for Plasma Theory and Computation,* 1500 *Engineering Drive, Madison, WI* 53706, *USA*
[2)] *Department of Physics, University of Wisconsin-Madison,* 1150 *University Avenue, Madison, WI* 53706, *USA*
[3)] *Department of Engineering-Physics, University of Wisconsin-Madison,* 1500 *Engineering Drive, Madison, WI* 53706, *USA*

The evolution of magnetic energy, helicity, and hybrid helicity during nonlinear relaxation of a driven-damped plasma pinch are compared in visco-resistive MHD and two-fluid models with and without the ion gyroviscous stress tensor. Magnetic energy and helicity are supplied via a boundary electric field which initially balances the resistive dissipation, and the plasma undergoes multiple relaxation events during the nonlinear evolution. The magnetic helicity is well conserved relative to the magnetic energy over each event, which is short compared to the global resistive diffusion time. The magnetic energy decreases by roughly 1.5% of its initial value over a relaxation event, while the magnetic helicity changes by at most 0.2% of the initial value. The hybrid helicity is dominated by magnetic helicity in low-β pinch conditions and is also well conserved. Differences of less than 1% between magnetic helicity and hybrid helicity are observed with two-fluid modeling and result from cross helicity evolution. The cross helicity is found to change appreciably due to the first-order finite Larmor radius effects which have not been included in contemporary relaxation theories. The plasma current evolves towards the flat parallel current state predicted by Taylor relaxation theory but does not achieve it. Plasma flow develops significant structure for two-fluid models, and the flow perpendicular to the magnetic field is much more substantial than the flow along it.

Submitted for publication to: *Physics of Plasmas*

[a)] Electronic mail: jpsauppe@gmail.com
[b)] Electronic mail: csovinec@wisc.edu

I. INTRODUCTION

The evolution of driven plasma pinch configurations, such as the reversed-field pinch (RFP) and spheromak, is characterized by the gradual accumulation and episodic release of free energy. The relaxation events involve rich macroscopic dynamics that couple multiple spatial scales and change the topology of magnetic field-lines while converting energy from one form to another. Theoretical efforts to describe the complicated evolution rest on constraints that take advantage of the separation of scales. Variational theories predict the outcome of relaxation events by minimizing free energy while maintaining the initial value of robust constraints. The variational theories based on static magnetohydrodynamics (MHD) are well known.[1,2] More recent developments consider plasma flow[3,4] and two-fluid effects that are outside the scope of the MHD model.[5–8]

Here, we examine the evolution of magnetic energy and generalized global helicities, as predicted in single- and two-fluid numerical models of relaxation dynamics with and without the ion gyroviscosity, a first-order finite Larmor radius (FLR) effect. Ion FLR effects are not included in existing relaxation theories, and ion gyroviscosity has been suggested as one possible avenue towards obtaining better agreement with experimental measurements.[9] Our primary goal is to understand the numerically predicted dynamics, as applied to conditions of magnetic confinement. We analyze the computed evolution of energy and components of helicity according to the different models and identify the contributions that cause deviation from ideal behavior. The computations allow evaluation of individual terms in the temporal rate of change of these quantities, and the relative importance of each term in the evolution is ascertained. The coupling between various pieces of the hybrid helicity in two-fluid models is also analyzed.

Invariants of ideal single-fluid MHD include the total energy, $W = W_B + W_K + W_P$, and the global magnetic helicity, $\mathcal{K} \equiv \int \boldsymbol{A} \cdot \boldsymbol{B}\, d^3x$ where $\boldsymbol{A}$ is the magnetic vector potential ($\boldsymbol{B} = \boldsymbol{\nabla} \times \boldsymbol{A}$), a topological measure of the magnetic field structure.[1,10] The magnetic helicity is ideally invariant in a closed system with a suitable choice for the gauge.[11,12] The physical justification for conserving helicity while minimizing energy comes from recognizing that turbulence in a plasma dissipates magnetic energy more readily than the global magnetic helicity.[13] Conserving magnetic helicity and minimizing magnetic energy yields the force-free relaxed state, $\boldsymbol{\nabla} \times \boldsymbol{B} = \lambda_0 \boldsymbol{B}$ with λ_0 a global constant. For sufficiently large current, the Taylor model predicts magnetic field reversal, a hallmark of RFP experiments.[2,14]

The Taylor theory does not address plasma flows which are observed in experimental plasmas even in the absence of any external sources of momentum.[15,16] Flow can be incorporated into a variational treatment through the cross helicity, $\mathcal{X} \equiv \int \boldsymbol{V} \cdot \boldsymbol{B}\, d^3x$.[3,5,17,18] The cross helicity is not conserved in general in single-fluid MHD, but it is conserved when certain restrictions are placed on the thermodynamic evolution.[19] Minimizing magnetic and kinetic energy while separately conserving the magnetic helicity and cross helicity yields a prediction for the relaxed state with both field-aligned currents, $\boldsymbol{\nabla} \times \boldsymbol{B} = \lambda_0 \boldsymbol{B}$, and flows, $m_i n \boldsymbol{V} = \lambda_1 \boldsymbol{B}$ where λ_1 is another global constant.

Dynamically, effects outside of the single-fluid MHD model couple current and flow during relaxation. Two-fluid effects in the generalized Ohm's law, the constitutive relation for the electric field in terms of the plasma variables, naturally couple current and flow. These effects become important when the ion and electron motions decouple, which occurs on scales below the ion-skin depth, $d_i \equiv c/\omega_{pi}$.[20–22] Coupling of current and flow relaxation is observed in numerical computations: substantial changes in plasma flow result with a two-fluid Ohm's law, whereas little change occurs with a single-fluid response.[23]

Extending the generalized Ohm's law to include two-fluid effects alters the evolution of the cross helicity. It is not an ideal invariant in the same limits as in single-fluid MHD.[5,24] An invariant of the incompressible Hall-MHD system of equations is the hybrid helicity $H \equiv \int \boldsymbol{\Omega} \cdot \boldsymbol{\nabla} \times \boldsymbol{\Omega}\, d^3x$ where $\boldsymbol{\Omega} \equiv \boldsymbol{A} + \frac{m_i}{e} \boldsymbol{V}$. The hybrid helicity measures the linking of canonical flux tubes and limits to the usual magnetic helicity as $d_i \to 0$. Expanding the product with the appropriate boundary conditions, the hybrid helicity appears as a weighted sum, $H = \mathcal{K} + 2\frac{m_i}{e}\mathcal{X} + \left(\frac{m_i}{e}\right)^2 \mathcal{H}$, where $\mathcal{H} \equiv \int \boldsymbol{V} \cdot \boldsymbol{\omega}\, d^3x$ is the kinetic helicity (with $\boldsymbol{\omega} \equiv \boldsymbol{\nabla} \times \boldsymbol{V}$), which measures the linkedness of fluid vorticity.[10]

The magnetic helicity and hybrid helicity are the limiting values of the canonical species' helicities (also called self helicities or generalized species' helicities) $\mathcal{K}_s \equiv \int \boldsymbol{A}_s \cdot \boldsymbol{B}_s\, d^3x$ for $\boldsymbol{A}_s = \boldsymbol{A} + \frac{m_s}{q_s} \boldsymbol{V}_s$ and $\boldsymbol{B}_s = \boldsymbol{\nabla} \times \boldsymbol{A}_s$,[6,7,25] where $s = i, e$. In the $m_e \to 0$ limit, $\mathcal{K}_e \to \mathcal{K}$ and $\mathcal{K}_i \to H$. The $\mathcal{K}_s$ are the ideal invariants of the more primitive two-fluid system of equations with a barotropic pressure for each species, $p_s = p_s(n_s)$.[9] Variational principles that minimize the total energy while conserving the $\mathcal{K}_{i,e}$ predict field-aligned currents and flows to lowest order in the species' skin depths, $d_{i,e}/a$,[7] similar to the previous single-fluid MHD results with cross helicity.

Two-fluid effects represent a singular perturbation of the single-fluid system, and these theories are singular in the $d_s \to 0$ limit. Variational theories with constraints that are more fragile than the target functional are mathematically ill-posed.[26–28] The kinetic helicity is a more fragile quantity than the kinetic energy, and relaxation theories that include kinetic helicity as a constraint while minimizing energy are not well posed. Different target functionals have been suggested,[26] but their physical motivation is not evident.[4] Rather than focusing on the mathematical validity of various relaxation theories, we investigate how the quantities that are utilized in these theories evolve during simulated relaxation events with experimentally relevant two-fluid parameters.

We choose to consider evolution in the RFP, which often displays multiple quasi-periodic relaxation events during a single discharge.[15] The RFP confines plasma primarily using magnetic fields generated by currents in the plasma itself, and the large magnetic shear and inductive toroidal current-drive result in parallel current being preferentially driven in the core of the device. The resulting gradient provides free energy for instabilities that nonlinearly saturate by redistributing the parallel current and relaxing the gradient.[29] Resistive diffusion and the inductive drive rebuild the current gradient, and the whole relaxation process may then be repeated. Measurements on the Madison Symmetric Torus[30] (MST) RFP demonstrate that the magnetic helicity is more robustly conserved than the magnetic energy over a relaxation event.[31] In addition, the changes in plasma flow are related to discrete current relaxation events,[15,16] and the parallel flow profile is observed to flatten during these events, as evident in Fig. 4(a) of Ref. 16. However, the kinetic energy is typically much smaller than the magnetic energy in magnetic confinement systems, and the parallel flow in MST is a small fraction of the Alvén velocity, $V_\parallel/V_A \sim 10^{-2}$. The free energy available from gradients in parallel current density is proportionately larger than the energy available from gradients in plasma flow, and the magnetics are expected to dominate the relaxation dynamics.

The remainder of the paper is organized as follows. The extended MHD model, initial and boundary conditions, and simulation parameters are described in Sec. II. In Sec. III, a theoretical analysis of the evolution of the quantities of interest in relaxation theories is presented, and the conditions required for each to be an ideal invariant are discussed. Particular focus is given to the coupling of various terms in the hybrid helicity in systems with two-fluid effects. The computational results are presented in Sec. IV, followed by a discussion and conclusions in Sec. V.

II. EXTENDED MHD MODEL

A. Model System

We investigate plasma relaxation dynamics numerically with the NIMROD code, which is used to solve extended MHD systems of equations,[32,33]

$$\frac{\partial n}{\partial t} = -\boldsymbol{\nabla}\cdot(n\boldsymbol{V}) + \boldsymbol{\nabla}\cdot(D_n\boldsymbol{\nabla}n) \tag{1}$$

$$m_i n\frac{\partial \boldsymbol{V}}{\partial t} = -m_i n\boldsymbol{V}\cdot\boldsymbol{\nabla}\boldsymbol{V} + \boldsymbol{F} \tag{2}$$

$$\begin{aligned} n\frac{\partial T}{\partial t} = &-n\boldsymbol{V}\cdot\boldsymbol{\nabla}T - nT(\Gamma-1)\boldsymbol{\nabla}\cdot\boldsymbol{V} \\ &+\boldsymbol{\nabla}\cdot(\chi n\boldsymbol{\nabla}T) \end{aligned} \tag{3}$$

$$\frac{\partial \boldsymbol{B}}{\partial t} = -\boldsymbol{\nabla}\times\boldsymbol{E} + \kappa\boldsymbol{\nabla}(\boldsymbol{\nabla}\cdot\boldsymbol{B}). \tag{4}$$

A small artificial number density diffusion term is included in the density evolution for numerical stability, but it does not enter directly into the evolution of the quantities of interest. Detailed thermal transport dynamics are not considered here, and a single temperature is used ($p_{i,e} = p/2$) with isotropic thermal conduction to provide some diffusion. In addition, viscous and Ohmic heating effects are neglected in the temperature equation, as the relaxation dynamics under investigation occur much faster than the transport time scales associated with those terms. Lastly, the NIMROD representation of fields does not satisfy $\boldsymbol{\nabla}\cdot\boldsymbol{B} = 0$ identically, so a divergence cleaning term is used with high-order spatial representation.[32] The influence of this numerical term on the evolution of magnetic energy, magnetic helicity, and cross helicity is quantified and discussed in Sec. IV.

The electric field is described by the generalized Ohm's law

$$\begin{aligned} \boldsymbol{E} = &-\boldsymbol{V}\times\boldsymbol{B} + \eta\boldsymbol{J} \\ &+\Lambda_e\left[\frac{\boldsymbol{J}\times\boldsymbol{B}}{ne} - \frac{\boldsymbol{\nabla}p_e}{ne} + \frac{m_e}{ne^2}\frac{\partial \boldsymbol{J}}{\partial t}\right]. \end{aligned} \tag{5}$$

The marker Λ_e is inserted to indicate where two-fluid effects enter the generalized Ohm's law; $\Lambda_e = 0$ for single-fluid MHD while $\Lambda_e = 1$ for two-fluid models. The first two terms on the right-hand side of Eq. (5) represent the standard MHD response. Measurements on the MST indicate that these terms alone are inadequate for a complete description of the physics of interest.[34] The first and third terms can be combined as $-\boldsymbol{V}\times\boldsymbol{B} + 1/ne\ \boldsymbol{J}\times\boldsymbol{B} = -\boldsymbol{V}_e\times\boldsymbol{B}$. To the extent that the remaining terms are small, the magnetic field is frozen into the electron fluid.

Electron inertia allows collisionless reconnection when the tearing layer width approaches the electron skin depth $\delta \sim d_e \equiv c/\omega_{pe}$.[20,35] We include it in the model equations to provide a resonance condition for the whistler wave at

the electron cyclotron frequency in order to limit the range of temporal scales as spatial resolution is increased.[33] It is measured to have negligible effect on the evolution of the quantities of interest in the computations that are presented.

The center-of-mass force density is

$$\begin{aligned}\boldsymbol{F} =& \boldsymbol{J}\times\boldsymbol{B} - \boldsymbol{\nabla}p \\ & - \boldsymbol{\nabla}\cdot\underline{\boldsymbol{\Pi}}_{\rm iso} - \Lambda_i\boldsymbol{\nabla}\cdot\underline{\boldsymbol{\Pi}}_{\rm gyr}\end{aligned} \tag{6}$$

where the marker Λ_i is used to indicate where ion FLR effects enter the system; $\Lambda_i = 0$ when they are excluded and $\Lambda_i = 1$ when they are included. If the ions are not cold, these effects enter at the same order as the drift effects in Ohm's law, and they can be included to first order via the Braginskii ion gyroviscous stress tensor,[36]

$$\begin{aligned}\underline{\boldsymbol{\Pi}}_{\rm gyr} = \frac{m_i p_i}{4e|\boldsymbol{B}|}\Big[&\hat{\boldsymbol{b}}\times\underline{\boldsymbol{W}}\cdot\left(\underline{\boldsymbol{I}}+3\hat{\boldsymbol{b}}\hat{\boldsymbol{b}}\right) \\ &-\left(\underline{\boldsymbol{I}}+3\hat{\boldsymbol{b}}\hat{\boldsymbol{b}}\right)\cdot\underline{\boldsymbol{W}}\times\hat{\boldsymbol{b}}\Big]\end{aligned} \tag{7}$$

where $\underline{\boldsymbol{W}} = \boldsymbol{\nabla}\boldsymbol{V}+(\boldsymbol{\nabla}\boldsymbol{V})^T-\frac{2}{3}\underline{\boldsymbol{I}}\,(\boldsymbol{\nabla}\cdot\boldsymbol{V})$ and $\hat{\boldsymbol{b}}\equiv\boldsymbol{B}/|\boldsymbol{B}|$. The gyroviscous stress tensor is non-dissipative and represents gyro-orbit frequency shifts and ellipticity resulting from $\boldsymbol{\nabla}\boldsymbol{E}$.[37] We also include a simple collisional viscosity in the model, $\underline{\boldsymbol{\Pi}}_{\rm iso} = \nu m_i n\underline{\boldsymbol{W}}$.

Turner[5] introduced the hybrid helicity for a similar Hall-MHD system of equations that includes two-fluid effects in the generalized Ohm's law ($\Lambda_e = 1$). However, he considered massless electrons ($m_e = 0$), so the electron inertia term is not present in his system. In addition, he assumed cold ions ($p_i = 0$), so FLR effects did not enter into his momentum equation ($\Lambda_i = 0$). Our use of a single temperature precludes an exact match to Turner's system even in the limit that $m_e \to 0$.

B. Initial and Boundary Conditions

We model the RFP dynamics in periodic cylinder geometry with minor radius a and axial length $L = 2\pi R$. The aspect ratio is $R/a = 3$, which is chosen to roughly match MST. The initial condition for the computations is a force-free paramagnetic pinch, $\boldsymbol{J}\times\boldsymbol{B}|_{t=0} = \boldsymbol{\nabla}p|_{t=0} = \boldsymbol{0}$, with finite plasma pressure. It is an Ohmic steady state that is sustained self-consistently by an externally applied electric field, $\boldsymbol{E}|_{t=0} = -\boldsymbol{V}\times\boldsymbol{B}|_{t=0}+\eta\boldsymbol{J}|_{t=0}$, with $\boldsymbol{\nabla}\times\boldsymbol{E}|_{t=0} = \boldsymbol{0}$.[38] This sustains the plasma current against resistive decay and injects both magnetic energy and magnetic helicity into the system. It is directed along the axis of the cylinder and is constant in time, and the normal component of magnetic field is held fixed, $\frac{\partial}{\partial t}\boldsymbol{B}\cdot\hat{\boldsymbol{n}}|_{r=a} = 0$, with $\boldsymbol{B}\cdot\hat{\boldsymbol{n}}|_{r=a,t=0} = 0$. Parallel current is preferentially driven in the plasma core, where the magnetic field is mostly aligned with $\boldsymbol{E}$, leading to a peaked parallel current profile that provides free energy for plasma instabilities.

The electric field drives a small radially inward pinch flow which is directly proportional to the plasma resistivity, and contributions from this term in the computations are verified to be small. No-slip boundary conditions are imposed on the tangential components of plasma flow. The temperature is held fixed at the boundary, $\frac{\partial}{\partial t}T|_{r=a} = 0$, and thermal energy may flow into and out of the system, although this rate is limited by the small isotropic thermal conductivity. With the artificial density diffusion, it is mathematically acceptable to utilize similar boundary conditions for the number density, $\frac{\partial}{\partial t}n|_{r=a} = 0$. As a result, particles may enter or exit the computational domain, but this also occurs on a much longer time-scale than the relaxation dynamics of interest.

C. Parameters

There are seven dimensionless physical parameters and two numerical parameters in the model equations (Eqs. (1)-(6)). The characteristic length scale is taken to be the plasma minor radius a. The seven physical parameters are (1) the Lundquist number, the ratio of the Alfvén time to the resistive diffusion time, $S = \tau_R/\tau_A$, where $\tau_A = a\sqrt{\mu_0 m_i n}/|\boldsymbol{B}|$ and $\tau_R = \mu_0 a^2/\eta$; (2) the magnetic Prandtl number, the ratio of resistive to viscous times, $P_m = \tau_R/\tau_\nu$, where $\tau_\nu = a^2/\nu$; (3) the ratio of the viscous to thermal conduction times, $\tau_\nu/\tau_\chi = \chi/\nu$; (4) the plasma-$\beta$, the ratio of fluid pressure to magnetic pressure, $\beta = 2\mu_0 p/B^2$; (5) the ion temperature fraction f_{T_i}; (6) the normalized ion skin depth, $d_i/a = c/\omega_{pi}a = \sqrt{m_i/\mu_0 ne^2}/a$; and (7) the normalized electron skin depth, $d_e/a = c/\omega_{pe}a = \sqrt{m_e/m_i}d_i/a$, which can be varied artificially by changing the mass ratio m_e/m_i. The two numerical parameters are (1) the ratio of viscous to density diffusion times, $\tau_\nu/\tau_{D_n} = D_n/\nu$; and (2) the ratio of divergence cleaning to resistive diffusion times, $\tau_{\boldsymbol{\nabla}\cdot\boldsymbol{B}}/\tau_R = \eta/\mu_0\kappa$.

All computations have $P_m = 1.0$, $\tau_\nu/\tau_\chi = 0.1$, $\beta = 0.10$ on axis, $d_i/a \approx 0.17$, $f_{T_i} = 0.5$ and $m_e/m_i \approx 2.72 \cdot 10^{-3}$. The on-axis plasma-$\beta$ is slightly higher than in the MST experiment, but the ion skin depth is comparable to estimates based on experimental values. The electron mass is artificially increased by a factor of 5 for numerical convenience.

Four distinct models under different physical conditions, summarized in Table I, are analyzed. The first model (A)

TABLE I. Parameters of models used in our computations.

Model	Λ_e	Λ_i	S	$a\lambda\,(0)$
A	0	0	$20,000$	-3.88
B	1	0	$20,000$	-3.88
C	1	1	$20,000$	-3.88
D	1	1	$80,000$	3.88

uses the standard magnetohydrodynamic Ohm's law ($\Lambda_e = 0$) and excludes the ion gyroviscous stress tensor ($\Lambda_i = 0$). The remaining models all incorporate two-fluid effects in the generalized Ohm's law ($\Lambda_e = 1$). The second model (B) does not include the gyroviscous stress tensor ($\Lambda_i = 0$), while the the third (C) and fourth (D) do ($\Lambda_i = 1$). Model D is described in greater detail in Ref. 23. Models A, B, and C are run with Lundquist number $S = 20,000$ and model D is run with $S = 80,000$. These values are roughly 2 orders of magnitude smaller than in the experiment, as limited by computational practicalities.

At $t = 0$, the dimensionless parallel current density, $a\lambda = a\mu_0 \boldsymbol{J}\cdot\boldsymbol{B}/|\boldsymbol{B}|^2$, has an on-axis value of $a\lambda\,(0) = -3.88$ in models A-C and $a\lambda\,(0) = 3.88$ for model D. Consequently, the magnetic helicity is negative in models A-C and positive in model D, which will be important when considering the normalized evolution later. (The MST experiment is typically operated with negative parallel current.)

The spatial discretization in the NIMROD code uses a spectral-element expansion[32] for two directions with a Fourier representation in the third periodic direction. In the cylindrical geometry under consideration here, the spectral elements are used for the radial (r) and axial (z) directions. The azimuthal (poloidal) angle (θ) is represented by finite Fourier series, and the computations here use 6 harmonics, $0 \le m \le 5$, where m is the poloidal harmonic number. Periodic boundary conditions are imposed in the axial direction to yield a topologically toroidal domain. Regularity conditions are enforced at $r = 0$, and the boundary conditions described in Sec. II B are enforced at $r = a$. The $r - z$ plane is discretized with a rectangular grid consisting of uniformly spaced elements in the radial and axial directions, with basis functions of fixed polynomial degree within each element.

Computations for models A, B, and C use 120 radial and 64 axial finite elements. Convergence is tested for these three models using basis functions of polynomial degree 3 and polynomial degree 5 within each element. The polynomial degree 5 results are presented in the main text of the paper, while the polynomial degree 3 cases are discussed briefly in Appendix B. The numerical parameters for models A, B, and C are $\tau_\nu/\tau_{D_n} = 0.1$ and $\tau_{\boldsymbol{\nabla}\cdot\boldsymbol{B}}/\tau_R = 5 \cdot 10^{-5}$. The $S = 80,000$ model D computation uses 240 radial and 60 axial finite elements with polynomial degree 4 and $\tau_{\boldsymbol{\nabla}\cdot\boldsymbol{B}}/\tau_R = 1.25 \cdot 10^{-5}$.

III. ENERGY AND HELICITY EVOLUTION

Before presenting the computational results, we present a brief analysis of how the magnetic energy, magnetic helicity, and hybrid helicity evolve within the model Eqs. (1)-(6). Knowledge of how the various components of the hybrid helicity couple with each other and under what conditions they are expected to be invariant is useful in understanding our numerical results.

A. Magnetic Energy

The global magnetic energy, $W_B = \int |\boldsymbol{B}|^2/2\mu_0 \; d^3x$, is minimized in many relaxation theories.[2,3,5,9] Using Eqs. (4)-(5), the magnetic energy evolves as

$$\frac{\partial W_B}{\partial t} = \int \left\{ -\boldsymbol{\nabla}\cdot\left(\frac{\boldsymbol{E}\times\boldsymbol{B}}{\mu_0}\right) - \eta J^2 + \boldsymbol{V}\times\boldsymbol{B}\cdot\boldsymbol{J} + \Lambda_e\left[\boldsymbol{J}\cdot\frac{\boldsymbol{\nabla}p_e}{ne} - \frac{m_e}{ne^2}\frac{\partial \boldsymbol{J}}{\partial t}\cdot\boldsymbol{J}\right] - \frac{\kappa}{\mu_0}\left(\boldsymbol{\nabla}\cdot\boldsymbol{B}\right)^2 \right\} d^3x. \tag{8}$$

The magnetic energy is not an ideal invariant alone; it couples to the kinetic energy through the MHD term $\boldsymbol{V}\times\boldsymbol{B}\cdot\boldsymbol{J}$, and only the total energy, $W_{\text{total}} = W_B + W_K + W_P$, is an ideal invariant. However, the magnetic energy is the dominant piece of the magnetofluid energy for our low-β pinch conditions, $W_{\text{mf}} \equiv W_B + W_K \approx W_B$. The Poynting flux on the

right-hand side represents the injection of magnetic energy through the driving electric field on the boundary, and the resistive dissipation exactly balances this in the initial paramagnetic pinch state.

The two-fluid terms ($\Lambda_e = 1$) couple to the electron thermal energy and the electron kinetic energy respectively. The use of a single temperature and the neglect of additional terms in the momentum equation renders these terms anomalous sources or sinks of magnetic energy.[39] However, these effects are small in our computations.

We note that the numerical divergence cleaning term can act as an anomalous loss of magnetic energy because the solenoidal and irrotational parts of the computed $\boldsymbol{B}$ are not completely independent. The separation improves with increasing spatial resolution, however.[32]

B. Magnetic Helicity

The global magnetic helicity is well conserved relative to magnetic energy in a weakly dissipative plasma[13] and is conserved in many variational theories (for example, Refs. 2, 3, and 5). We use a gauge-invariant relative magnetic helicity,[25] $\mathcal{K} = \int (\boldsymbol{A} - \boldsymbol{A}') \cdot (\boldsymbol{B} + \boldsymbol{B}') \; d^3x$, which evolves as

$$\frac{\partial \mathcal{K}}{\partial t} = 2 \int \left\{ \boldsymbol{\nabla} \cdot (\boldsymbol{A}' \times \boldsymbol{E}') - \eta \boldsymbol{J} \cdot \boldsymbol{B} + \frac{\kappa}{2} \boldsymbol{A} \cdot \boldsymbol{\nabla} (\boldsymbol{\nabla} \cdot \boldsymbol{B}) + \Lambda_e \left[\boldsymbol{B} \cdot \frac{\boldsymbol{\nabla} p_e}{ne} - \frac{m_e}{ne^2} \frac{\partial \boldsymbol{J}}{\partial t} \cdot \boldsymbol{B} \right] \right\} d^3x. \tag{9}$$

The reference magnetic field, $\boldsymbol{B}' = \boldsymbol{\nabla} \times \boldsymbol{A}'$, is chosen to be the vacuum field with $(\boldsymbol{A} - \boldsymbol{A}') \times \hat{\boldsymbol{n}}|_{r=a} = \boldsymbol{0}$ and $(\boldsymbol{E} - \boldsymbol{E}') \times \hat{\boldsymbol{n}}|_{r=a} = \boldsymbol{0}$. The reference field is steady, $\frac{\partial}{\partial t} \boldsymbol{B}' = -\boldsymbol{\nabla} \times \boldsymbol{E}' = \boldsymbol{0}$.

In a single-fluid MHD model, only the first two terms on the right remain, and the magnetic helicity is invariant in the ideal limit when both vanish. The first term represents injection of helicity from the boundary while the second represents resistive dissipation, and they exactly balance in the initial state in our computations.

In a two-fluid model ($\Lambda_e = 1$, $\kappa = 0$), the magnetic helicity is not an ideal invariant, unless the electron mass is ignored and the electron pressure is barotropic, $p_e = p_e(n)$.[5,9] The electron pressure term couples magnetic helicity to cross helicity only for models with two-fluid effects, as will be seen next. The numerical divergence cleaning term here allows unphysical changes in magnetic helicity, and it is not guaranteed to be a sink.

C. Flow Invariants

Plasma flow is incorporated in variational theories by including the cross helicity, $\mathcal{X} = \int \boldsymbol{V} \cdot \boldsymbol{B} \; d^3x$, as a conserved quantity.[3,5,28] Including a weighting factor, $2\frac{m_i}{e}$, the weighted cross helicity ($\hat{\mathcal{X}} \equiv 2\frac{m_i}{e}\mathcal{X}$) evolves as

$$\begin{aligned} \frac{\partial \hat{\mathcal{X}}}{\partial t} = 2 \int \Bigg\{ & - \frac{m_i}{e} \boldsymbol{\omega} \cdot \left[\eta \boldsymbol{J} + \Lambda_e \left(\frac{\boldsymbol{J} \times \boldsymbol{B}}{ne} - \frac{\boldsymbol{\nabla} p_e}{ne} + \frac{m_e}{ne^2} \frac{\partial \boldsymbol{J}}{\partial t} \right) \right] \\ & - \boldsymbol{B} \cdot \left[\frac{\boldsymbol{\nabla} \cdot \underline{\boldsymbol{\Pi}}_{\text{iso}}}{ne} + \Lambda_i \frac{\boldsymbol{\nabla} \cdot \underline{\boldsymbol{\Pi}}_{\text{gyr}}}{ne} + \frac{\boldsymbol{\nabla} p_e}{ne} + \frac{\boldsymbol{\nabla} p_i}{ne} \right] + \kappa \frac{m_i}{e} \boldsymbol{V} \cdot \boldsymbol{\nabla} (\boldsymbol{\nabla} \cdot \boldsymbol{B}) \Bigg\} d^3x. \end{aligned} \tag{10}$$

The electron pressure gradient parallel to the magnetic field is present regardless of the form of the generalized Ohm's law, but it couples to the magnetic helicity evolution only when two-fluid effects are included in the model.

Consider first a single-fluid MHD model ($\Lambda_e, \Lambda_i \to 0$). In the ideal ($\eta, \nu, \kappa \to 0$) limit, the cross helicity evolution only depends on the gradient of the total pressure along the magnetic field. It is only an ideal invariant for a single-fluid model when restrictions are placed on the thermodynamic evolution, such as negligible plasma pressure or a barotropic response. Note that an estimate of the resistive term here yields $\frac{\partial}{\partial t}\mathcal{X} \sim \eta \boldsymbol{J} \cdot \boldsymbol{\nabla} \times \boldsymbol{V} \sim \sum_k \eta k^2 v_k B_k$ while a similar analysis[13] of the resistive term in the magnetic energy evolution results in $\frac{\partial}{\partial t} W_B \sim \eta J^2 \sim \sum_k \eta k^2 B_k^2$. A comparison of these terms shows that cross helicity is not conserved to a greater degree than the magnetic energy in a resistive plasma.[27]

In models that include two-fluid effects ($\Lambda_e = 1$), the cross helicity is not an ideal invariant, even with restrictions on plasma pressure. Turner[5] recognized that a conserved quantity can be constructed for certain two-fluid models using the kinetic helicity, $\mathcal{H} = \int \boldsymbol{V} \cdot \boldsymbol{\omega} \; d^3x$ with $\boldsymbol{\omega} \equiv \boldsymbol{\nabla} \times \boldsymbol{V}$, as part of a weighted sum. In our model equations, the weighted kinetic helicity ($\hat{\mathcal{H}} \equiv \left(\frac{m_i}{e}\right)^2 \mathcal{H}$) evolves as

$$\frac{\partial \hat{\mathcal{H}}}{\partial t} = 2 \int \left\{ \left[\frac{\boldsymbol{J} \times \boldsymbol{B}}{ne} - \frac{\boldsymbol{\nabla} p_e}{ne} - \frac{\boldsymbol{\nabla} p_i}{ne} - \frac{\boldsymbol{\nabla} \cdot \underline{\boldsymbol{\Pi}}_{\text{iso}}}{ne} - \Lambda_i \frac{\boldsymbol{\nabla} \cdot \underline{\boldsymbol{\Pi}}_{\text{gyr}}}{ne} \right] \cdot \frac{m_i}{e} \boldsymbol{\omega} \right\} d^3x. \tag{11}$$

The first two terms on the right hand side are equal and opposite to the first two Λ_e terms in the cross helicity evolution, justifying the chosen weighting factors to effect a cancellation. The hybrid helicity is then constructed as a weighted sum of the magnetic, cross, and kinetic helicities: $H \equiv \mathcal{K} + 2\frac{m_i}{e}\mathcal{X} + \left(\frac{m_i}{e}\right)^2 \mathcal{H}$. Combining Eqs. (9), (10), and (11) yields the evolution of the hybrid helicity,

$$\begin{aligned}\frac{\partial H}{\partial t} = 2\int \Bigg\{ & \boldsymbol{\nabla}\cdot(\boldsymbol{A}'\times\boldsymbol{E}') + \kappa\left(\frac{\boldsymbol{A}}{2}+\frac{m_i}{e}\boldsymbol{V}\right)\cdot\boldsymbol{\nabla}(\boldsymbol{\nabla}\cdot\boldsymbol{B}) \\ & - \left(\boldsymbol{B}+\frac{m_i}{e}\boldsymbol{\omega}\right)\cdot\left[\eta\boldsymbol{J} + \frac{\boldsymbol{\nabla}\cdot\underline{\boldsymbol{\Pi}}_{\text{iso}}}{ne} + \frac{\boldsymbol{\nabla}p_i}{ne} + \Lambda_i\frac{\boldsymbol{\nabla}\cdot\underline{\boldsymbol{\Pi}}_{\text{gyr}}}{ne} + (\Lambda_e-1)\left(\frac{\boldsymbol{J}\times\boldsymbol{B}}{ne}-\frac{\boldsymbol{\nabla}p_e}{ne}\right) + \Lambda_e\frac{m_e}{ne^2}\frac{\partial\boldsymbol{J}}{\partial t}\right]\Bigg\} d^3x.\end{aligned} \tag{12}$$

The hybrid helicity is an ideal invariant in the two-fluid model considered by Turner ($\Lambda_e = 1$, $m_e = 0$, $p_i = 0$, $\Lambda_i = 0$, $\kappa = 0$). More generally, however, the hybrid helicity is not an invariant of the system of Eqs. (1)-(6), due to the FLR effects ($\Lambda_i = 1$), electron inertia ($m_e \neq 0$), and finite ion pressure ($p_i \neq 0$). The FLR effects on hybrid helicity evolution will be shown to be significant in our computations, and this provides additional motivation for the development of relaxation theories that include them.[9]

D. Hybrid Helicity Scaling

The relative importance of each component of the hybrid helicity can be inferred from simple scaling estimates. For the magnetic helicity, the dominant contribution comes from the large axisymmetric magnetic field as opposed to the turbulent correlations, and it scales as $\boldsymbol{A}\cdot\boldsymbol{B} \sim aB_0^2$, where the minor radius a is used as the characteristic length scale for $\boldsymbol{A}$. Flows are scaled by a characteristic flow velocity V_0, and the cross helicity contribution scales as $\frac{m_i}{e}\boldsymbol{V}\cdot\boldsymbol{B} \sim \left(aB_0^2\right)\left(\frac{m_i}{eB_0}\right)\frac{V_0}{a} \sim \left(aB_0^2\right)(d_i/a)(V_0/V_A)$ where V_A is the Alfvén velocity, $V_A \equiv B_0/\sqrt{\mu_0 m_i n}$. The fluid vorticity has no initial axisymmetric component, and it is expected to scale like $\boldsymbol{\omega} = \boldsymbol{\nabla}\times\boldsymbol{V} \sim kV_0$, where k represents the typical wavenumber of velocity fluctuations. The weighted kinetic helicity density is then $\left(\frac{m_i}{e}\right)^2\boldsymbol{V}\cdot\boldsymbol{\omega} \sim \left(aB_0^2\right)\left(\frac{m_i}{eB_0}\right)^2\frac{V_0^2}{a^2}(ka) \sim \left(aB_0^2\right)(d_i/a)^2(V_0/V_A)^2(ka)$.

Defining $\hat{\epsilon} \equiv (d_i/a)(V_0/V_A)$, the hybrid helicity can be written as

$$\frac{H}{aB_0^2} = \int \hat{\boldsymbol{A}}\cdot\hat{\boldsymbol{B}}\; d^3x + 2\hat{\epsilon}\int \hat{\boldsymbol{V}}\cdot\hat{\boldsymbol{B}}\; d^3x + \hat{\epsilon}^2(ka)\int \hat{\boldsymbol{V}}\cdot\hat{\boldsymbol{\omega}}\; d^3x. \tag{13}$$

If the characteristic flows are much less than an Alfvén speed $V_0/V_A \ll 1$ and the ion skin depth is not large compared to a characteristic length $d_i/a \ll 1$, then the hybrid helicity is dominated by the magnetic helicity. These conditions are typical for magnetic confinement. Also, the cross helicity contribution is an order of $\hat{\epsilon}^{-1}$ larger than the kinetic helicity contribution, assuming that ka does not scale as $\hat{\epsilon}^{-1}$.

IV. RESULTS

A. Global Evolution

All computations introduced in Sec. II C undergo at least one discrete relaxation event as the nonlinear dynamics rearrange the magnetic topology and reverse the axial magnetic field at the boundary relative to the initial paramagnetic pinch state. This is evident in the evolution of the dimensionless field reversal parameter and the normalized magnetic energy, magnetic helicity, and hybrid helicity, shown for our computations in Fig. 1. The magnetic and hybrid helicities are well conserved relative to the magnetic energy over each relaxation event, which lasts between 200 τ_A and 460 τ_A, a small fraction of a global resistive diffusion time for both the $S = 20,000$ and $S = 80,000$ computations. In the absence of two-fluid effects (A), the magnetic helicity ($\mathcal{K}$) and hybrid helicity (H) are nearly indistinguishable. When two-fluid effects are included (B, C, and D), the evolution of $\mathcal{K}$ and H differ, a result that is discussed in greater detail in Sec. IV C.

In computations A and B, the first event is qualitatively distinct from subsequent events as a result of the initial conditions. The initial paramagnetic pinch state is unstable to several different linear modes, and the fastest growing mode saturates nonlinearly before any other mode reaches appreciable amplitude. We define the start of the first

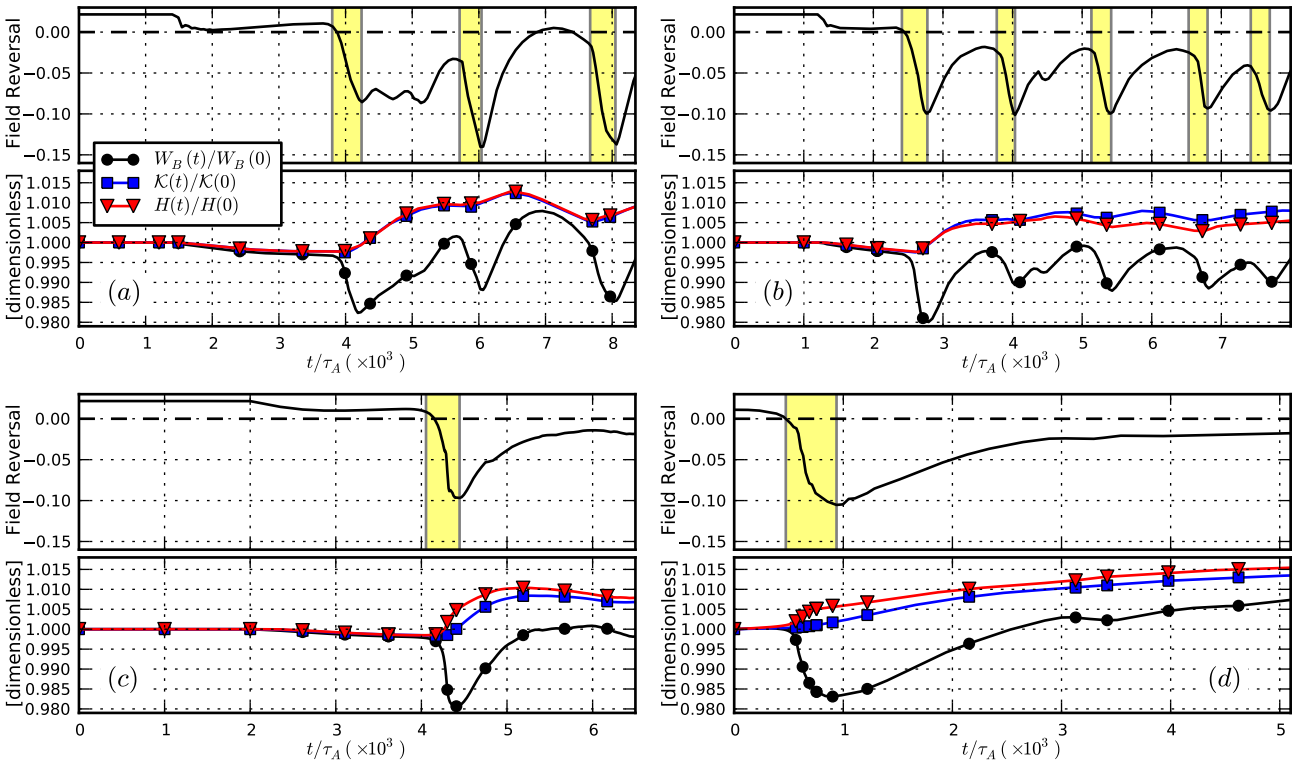

FIG. 1. Field reversal parameter and normalized magnetic energy $W_B(t)/W_B(0)$, magnetic helicity $\mathcal{K}(t)/\mathcal{K}(0)$, and hybrid helicity $H(t)/H(0)$ in (a) case A: single-fluid MHD, $\Lambda_e = 0$, $\Lambda_i = 0$, (b) case B: two-fluid no gyroviscosity, $\Lambda_e = 1$, $\Lambda_i = 0$, (c) case C: two-fluid with gyroviscosity $\Lambda_e = 1$, $\Lambda_i = 1$, and (d) case D: two-fluid with gyroviscosity $\Lambda_e = 1$, $\Lambda_i = 1$. The relaxation events are highlighted.

relaxation event as when the slower-growing modes contain approximately 5% of the energy of the dominant linearly unstable mode. The end of the relaxation event is determined when the field reversal parameter reaches a minimum, and this is nearly coincident with the minimum of magnetic energy in each case. The magnetic energy decreases substantially over the first event in all computations, $\Delta W_B/W_B(0) \approx -1.4\%$ to -1.7%, while the change in magnetic helicity is an order of magnitude smaller, $\Delta\mathcal{K}/\mathcal{K}(0) \approx 0.13 - 0.23\%$.

Subsequent relaxation events are observed in computations A and B, and are identified based on significant nonlinear correlations. In the single-fluid MHD computation (A), subsequent events occur roughly every 1900 τ_A, about a tenth of a resistive diffusion time for $S = 20,000$. The changes in magnetic energy and helicity are very similar to the first event. In our computation that includes two-fluid effects in the generalized Ohm's law only (B), subsequent relaxation events occur more frequently, with an average interval of 1300 τ_A. However, the magnetic energy loss in these later events is less severe, typically between 0.5% and 1.1%, with proportionately smaller changes in magnetic helicity of at most 0.05% over the event. Computations that include the ion gyroviscosity (C and D) show greatly reduced magnetic activity following the first event, and no subsequent large relaxation events are observed over the remainder of each computation. The ion gyroviscosity has a stabilizing effect on linear tearing modes in pinch configurations,[40] and this may be responsible for the less dynamic behavior following the initial relaxation event.

The recovery time scale, estimated by the time required for W_B to return to its pre-crash value, is set by the injection of magnetic energy through the boundary electric field, which scales inversely with S. In our $S = 20,000$ computations (A, B, and C), the recovery time scale is only somewhat larger than the relaxation time scale, but the recovery time scale is significantly longer at larger S. In case D, the duration of the relaxation event is 461 τ_A, comparable to the $S = 20,000$ cases, but the recovery process is 1582 τ_A, longer than in the lower Lundquist number cases. The drop in magnetic energy is nearly the same as in computation C, but the changes in magnetic helicity and hybrid helicity are slightly reduced. As the Lundquist number approaches more realistic values, the difference between the relaxation time scale and the recovery time scale is expected to increase even further.

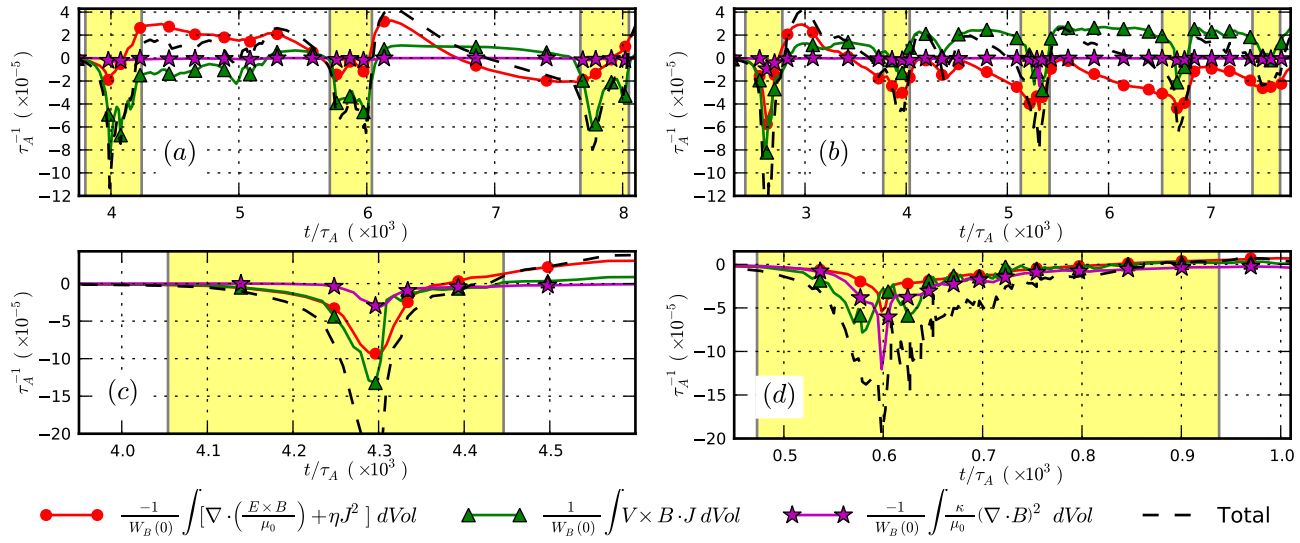

FIG. 2. Decomposition of magnetic energy evolution for (a) case A, (b) case B, (c) case C, and (d) case D. Note that axes differ.

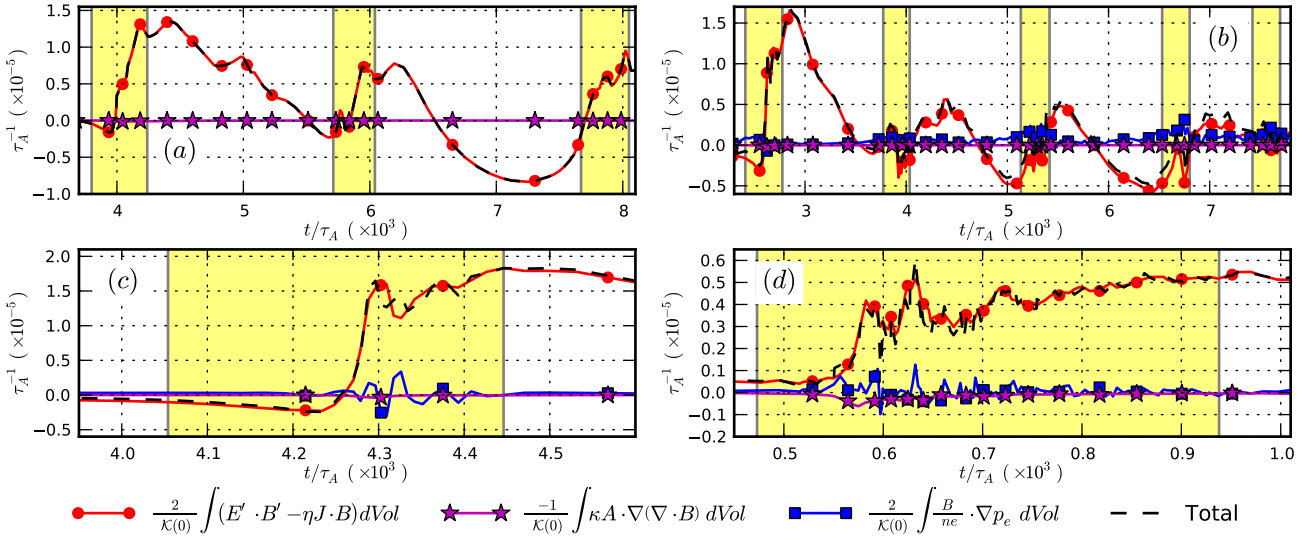

FIG. 3. Decomposition of magnetic helicity evolution for (a) case A, (b) case B, (c) case C, and (d) case D.

B. Analysis of Magnetic Energy and Helicity Evolution

Magnetic energy is converted into kinetic energy during a relaxation event, and it is lost to resistive dissipation. This can be seen in Fig. 2, which shows the dominant terms in the magnetic energy evolution (Eq. (8)) for our computations. The electron pressure and electron inertia terms in our two-fluid computations (B-D) are negligible and are not shown. Using $\int dt \int \boldsymbol{J}\cdot\boldsymbol{\nabla} p_e/ne\; d^3x$ as a gauge, where the temporal integration is over a relaxation event, we find that the neglect of separate temperatures for the electrons and ions does not substantially affect the evolution of magnetic energy. After the relaxation event, the magnetic energy recovers through the injection via the boundary electric field, which overcomes the resistive losses in the more relaxed profile. The coupling to kinetic energy has a more significant role in the recovery in subsequent relaxation events, especially in computation B.

The robustness of the magnetic helicity relative to the magnetic energy over a relaxation event is evident from Fig. 1. This property can also be seen by comparing the amplitudes in Fig. 3, which shows the dominant terms in the helicity evolution (Eq. (9)), to those in Fig. 2. The driving electric field injects magnetic helicity, and this balances the resistive dissipation across the plasma in the paramagnetic pinch initial conditions. However, as the plasma relaxes into a state of lower dissipation (when the red curves in Fig. 3 have positive values), the helicity within the plasma

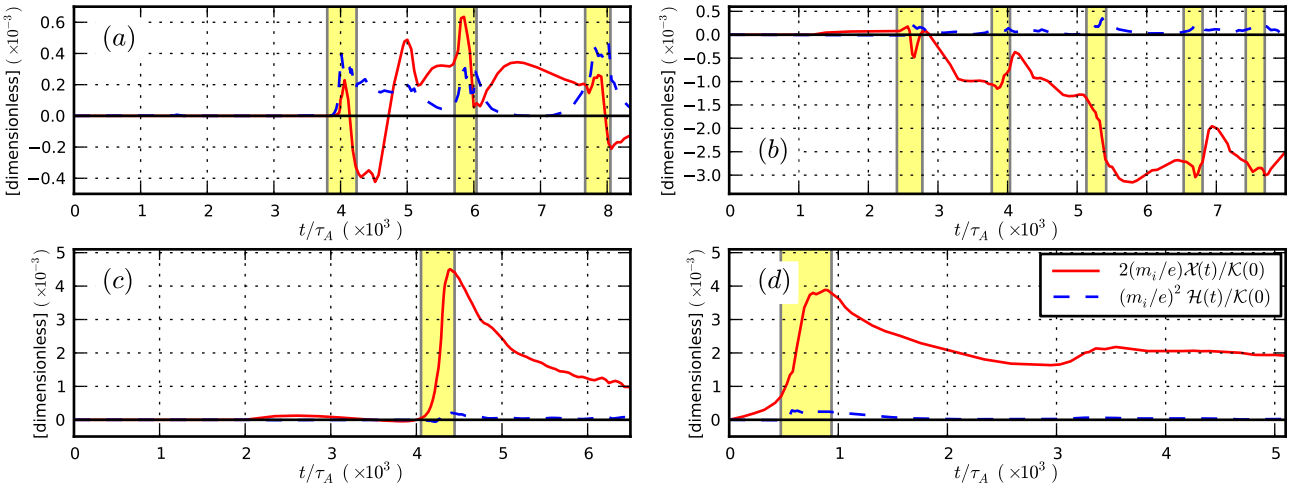

FIG. 4. Normalized cross helicity $2\frac{m_i}{e}\mathcal{X}(t)/\mathcal{K}(0)$, and kinetic helicity $\left(\frac{m_i}{e}\right)^2\mathcal{H}(t)/\mathcal{K}(0)$ for (a) case A, (b) case B, (c) case C, and (d) case D.

column increases on a resistive timescale. In our two-fluid computations, the coupling to cross helicity through the parallel electron pressure gradient is small over the first event, although it becomes somewhat significant afterwards in computation B, peaking during the subsequent events. The electron inertia term is negligible and is not shown.

The magnetic energy and helicity evolution are well resolved in our computations A, B, and C. This conclusion is based on a comparison of the importance of physical terms in the evolution to the numerical divergence cleaning term. An analysis of similar computations with lower spatial resolution, discussed briefly in Appendix B, provides further evidence for this conclusion. In these computations, the divergence cleaning accounts for at most 12.6% of the loss of magnetic energy over a relaxation event (which is about 1.5% of the total magnetic energy) and at most 1.5% of the roughly 0.2% net change in magnetic helicity. Applying a similar analysis to our computation D, we find that the magnetic helicity evolution is well resolved but the magnetic energy evolution is not. The divergence cleaning term accounts for 43.6% of the total loss of magnetic energy, $\Delta W_B/W_B(0) = -1.66\%$, although the total change is comparable to computation C with $\Delta W_B/W_B(0) = -1.70\%$. In spite of the numerical losses, computation D behaves very similarly to our computation C with its more easily resolved conditions.

C. Hybrid Helicity Evolution

The difference between hybrid helicity and magnetic helicity, $H - \mathcal{K} = 2\frac{m_i}{e}\mathcal{X} + \left(\frac{m_i}{e}\right)^2\mathcal{H}$, in our two-fluid computations is primarily due to the cross helicity. This can be seen in Fig. 4, which shows the evolution of the weighted cross and kinetic helicities. In all of our computations, the weighted kinetic helicity is small, and this reflects the orderings of Eq. (13). Flows in these computations are sub-Alfvénic, $|\boldsymbol{V}|/V_A \leq 0.02$, and the normalized ion skin depth is $d_i/a \approx 0.17$. Using the wavenumber for the dominant linear mode, $ka = a(m/r_s + k_z) \approx 10$, we obtain an estimate for the importance of each component: $\frac{m_i}{e}\mathcal{X}/\mathcal{K} \approx 3.4\cdot 10^{-3}$ and $\left(\frac{m_i}{e}\right)^2\mathcal{H}/\mathcal{K} \approx 1.2\cdot 10^{-4}$. Consequently, the evolution of $\mathcal{H}$ is not considered here.

In case A, the weighted cross helicity is also small relative to the dominant magnetic helicity ($|\hat{\mathcal{X}}|/\mathcal{K}(0) \lesssim 0.06\%$), and the hybrid helicity remains approximately equal to the magnetic helicity throughout the evolution. Computations that include two-fluid effects display changes in cross helicity that are roughly an order of magnitude greater than in the single-fluid MHD computation. Comparing case B ($\Lambda_i = 0$) and case C ($\Lambda_i = 1$), it is clear that the ion gyroviscosity has a substantial effect on cross helicity evolution, and this change is largely independent of resistivity between $S = 20,000$ and $S = 80,000$ (cases C and D). Recall that the initial value of the magnetic helicity, $\mathcal{K}(0)$, is negative for cases A-C and positive for case D; thus, the sign of $2\frac{m_i}{e}\mathcal{X}(t)/\mathcal{K}(0)$ is opposite to the cross helicity $\mathcal{X}(t)$ in cases A-C. Although $\mathcal{X}$ has the opposite sign in cases C and D, the magnitude of the change is similar; $|\hat{\mathcal{X}}|$ increases to approximately 0.5% of $|\mathcal{K}|$.

Cross helicity is conserved well in our computations without two-fluid effects, even without thermodynamic restrictions on pressure. The small changes in cross helicity in our single-fluid MHD computation (case A) are primarily due to the viscosity, as seen in Fig. 5, which shows the dominant terms in the cross helicity evolution, Eq. (10), for our computations. Here, the viscosity becomes most significant at the relaxation events, although it changes sign about

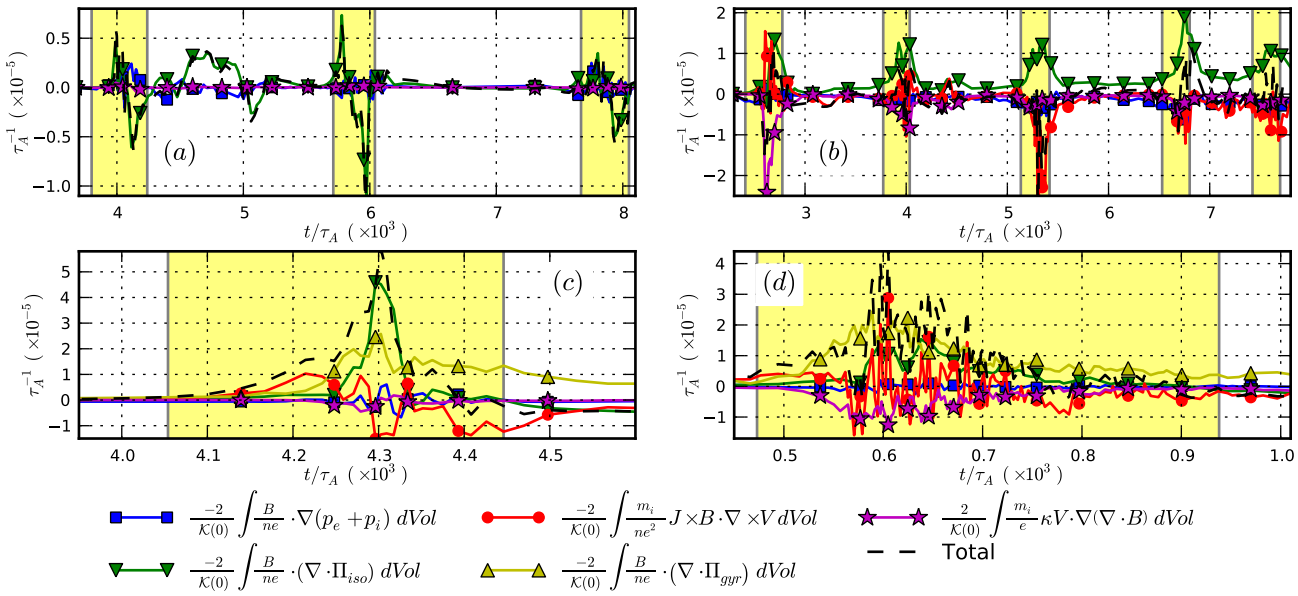

FIG. 5. Decomposition of cross helicity evolution for (a) case A, (b) case B, (c) case C, and (d) case D.

halfway through each event leading to little net change.

The two-fluid Hall term substantially affects cross helicity evolution in case B. During the first and second event, the viscosity and Hall effects generally reinforce each other, but the numerical divergence cleaning is also large in these events. Consequently, we can attach little physical significance to the cross helicity evolution here. However, in later events, which are better resolved, the two-fluid Hall term tends to drive the changes in cross helicity, and it is opposed by the viscosity. In addition, the pressure gradient along the magnetic field, which only couples cross helicity and magnetic helicity evolution for two-fluid models ($\Lambda_e = 1$), is also significant in these subsequent events in case B.

The ion gyroviscosity has a considerable effect on cross helicity evolution (cases C and D). The gyroviscous and viscous contributions both increase cross helicity during the relaxation, while the Hall term varies between reinforcement and opposition. The viscous effects are somewhat smaller in case D, which has a smaller isotropic viscosity coefficient, and the Hall term oscillates much more rapidly over the event. Shortly after relaxation, a balance is reached between the gyroviscosity and the remaining terms, and the cross helicity settles into a non-zero steady state. The divergence cleaning effects on cross helicity evolution in case D are comparable to the physical terms. However, the dynamics appear qualitatively consistent with the evolution in case C, which is well resolved. The ion gyroviscosity is responsible for large changes in the cross helicity at the relaxation event and breaks the invariance of the hybrid helicity when it is included in the model.

D. Current Relaxation

Since the magnetic helicity is well conserved relative to magnetic energy over a timescale that is short compared to the global resistive diffusion time, it is appropriate to compare to the predictions of relaxation theories discussed in Sec. I. Single-fluid theories[2,3] and two-fluid extensions[5,7,9] predict a completely flat parallel current profile, $\lambda = \mu_0 \boldsymbol{J}\cdot\boldsymbol{B}/|\boldsymbol{B}|^2 =$ constant, to lowest order in the species' skin-depths, $d_{i,e}/a$. In our computations, the normalized value of the magnetic helicity, $|\hat{\mathcal{K}}| = (a/R)\left(|\mathcal{K}|/\psi_{\rm tor}^2\right) = 5.3293$, is below the critical value of $\hat{\mathcal{K}}_{\rm crit} = 8.21$ that is required for an axisymmetric relaxed state.[41] As a result, the predicted relaxed state is axisymmetric with the dimensionless parallel current density $|\lambda a| = 2.916$.

The parallel current gradient is reduced during relaxation, and the profile is driven closer to the fully relaxed state. The relaxation over the first event can be seen in Fig. 6; the parallel current profile at the end of subsequent events is similar. In the initial paramagnetic pinch state, the parallel current is strongly peaked and is far from the predicted flat profile. Relaxation reduces parallel current in the core of the plasma, where $|\lambda a|$ exceeds the predicted relaxed state value, and increases it where $|\lambda a|$ is below it. However, the fully relaxed current state is never achieved. A large current gradient persists in the edge region after relaxation, similar to experimental results.[42,43] The boundary electric field drive and resistive diffusion slowly rebuild the peaked profile between events, and they drive the plasma

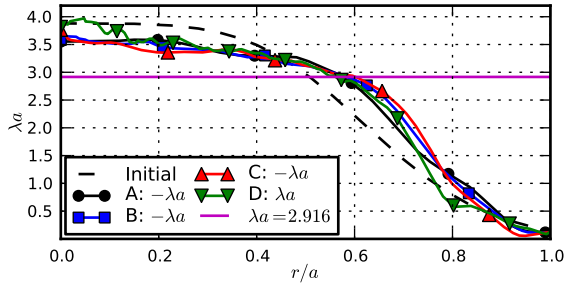

FIG. 6. Profile of dimensionless parallel current for the initial state, and at the end of the first relaxation event for cases A, B, C, and D. The flat parallel current Taylor state prediction is also shown.

further from the fully relaxed state and closer to the paramagnetic pinch Ohmic steady-state. Plasma instabilities may then initiate another nonlinear relaxation event, and the whole process may repeat quasi-periodically.

E. Flow Relaxation

Single-fluid MHD theories that include the cross helicity as a conserved quantity[3] predict both flat parallel current and momentum density that is aligned with $\boldsymbol{B}$, $m_i n \boldsymbol{V} = \lambda_1 \boldsymbol{B}$, where λ_1 is a global constant. Two-fluid theories that conserve the hybrid helicity,[5] although mathematically ill-posed,[26] predict relaxed states with more complicated flow structures. To lowest order in $d_{i,e}/a$, however, the flow is predicted to be parallel to the magnetic field.[7]

The computations presented here begin with no parallel flow across the plasma, but relaxation gives rise to parallel flow with significant radial structure, as seen in Fig. 7. The density fluctuations are small in our computations, and

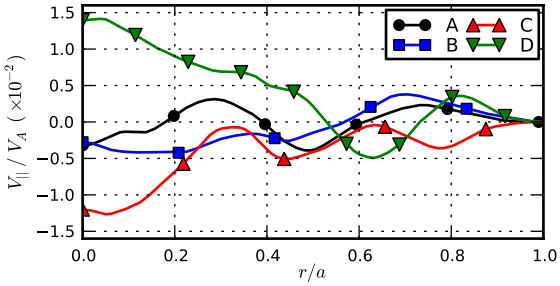

FIG. 7. Profile of $V_\parallel/V_A$ at the end of the first relaxation event for cases A, B, C, and D.

the structure of $nV_\parallel$ is very similar to that of $V_\parallel$. In Sec. IV F, we note that energy in the perpendicular part of the flow exceeds that of the parallel component. Clearly, these predictions for flow are not realized following relaxation events in our computations.

The cross helicity is most robustly conserved in case A, and here the generated parallel flow varies between negative and positive across the plasma. The magnitude of the parallel flow remains small, $|V_\parallel|/V_A \lesssim 0.5\%$, in agreement with results reported in Ref. 23. In our two-fluid computation without ion gyroviscosity (B), the cross helicity changes very little over the first event, and the magnitude of the parallel flow is comparable to case A. However, the physical terms in the cross helicity evolution are offset by numerical effects over the first event, and the significance of the parallel flow profile here is questionable. Subsequent relaxation events in case B are better resolved, and the magnitude of $\Delta V_\parallel/V_A$ over these events can be comparable to cases C and D. This can be seen in Fig. 8, which shows the parallel flow profile at the beginning and end of the third and fourth relaxation events in case B. The parallel flow continues to exhibit significant radial variation following the subsequent relaxation events and does not approach a uniform flow state. However, in these subsequent events, $\Delta V_\parallel/V_A > 0$ in the core, which contrasts with the behavior in the first event.

Based on empirical observations from our computational results in case B, changes in the local parallel flow profile do not appear to be well correlated with the changes in cross helicity. In the third relaxation event the cross helicity roughly doubles in magnitude, $\Delta\hat{\mathcal{X}}/\mathcal{K}(0) \sim -0.134\%$, but the changes in the parallel flow profile are small. The change in cross helicity is much smaller over the fourth event, $\Delta\hat{\mathcal{X}}/\mathcal{K}(0) \sim -0.001\%$, but the parallel flow profile

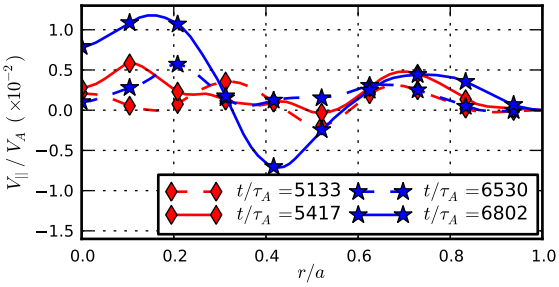

FIG. 8. Profile of $V_\parallel/V_A$ at the beginning and end of the third and fourth relaxation events in case B.

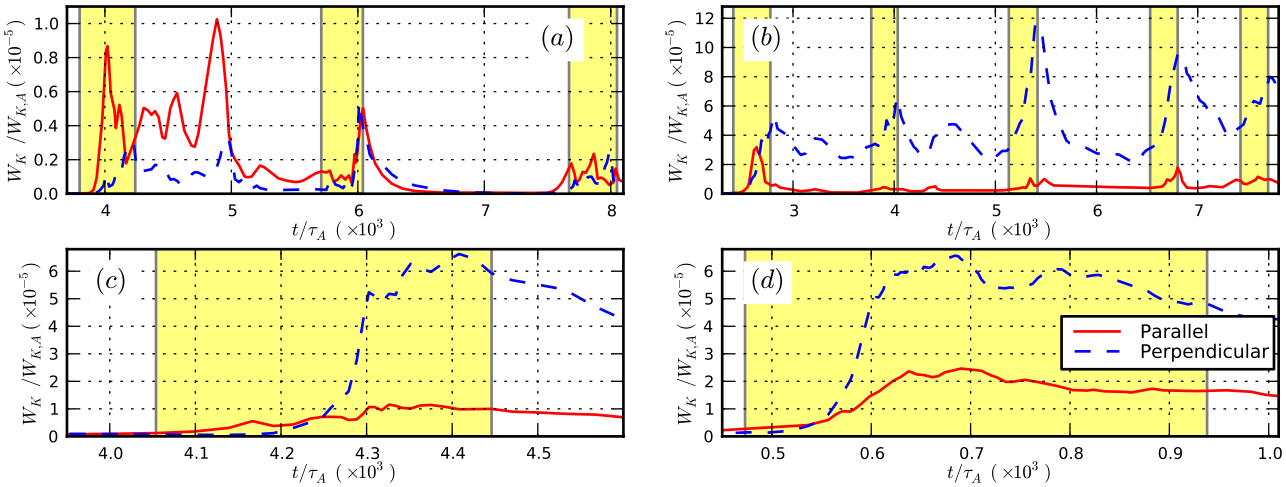

FIG. 9. Kinetic energy in component of flow parallel, $W_{K,\parallel} \equiv \int \frac{m_i}{2} \langle n \rangle \langle V_\parallel \rangle^2 d^3x$, and perpendicular, $W_{K,\perp} \equiv \int \frac{m_i}{2} \langle n \rangle \langle V_\perp \rangle^2 d^3x$, to the axisymmetric magnetic field, normalized by $W_{K,A} \equiv \int \frac{m_i}{2} n_0 V_A^2 d^3x$, for (a) case A, (b) case B, (c) case C, and (d) case D.

changes are much larger than in the third event.

In contrast to this, the changes in parallel flow and cross helicity appear well correlated in our computations that include both two-fluid effects and ion gyroviscosity (C and D). Both computations display large changes in cross helicity at the relaxation event, and the parallel flow profile after relaxation is strongly peaked in these computations. However, the direction of the generated parallel flow depends upon the initial parallel current density, which differs in cases C and D, and this provides evidence that changes in parallel flow are intrinsically related to current relaxation.

F. Kinetic Energy Evolution

Our computations display a strong anisotropy in the axisymmetric flow parallel to the axisymmetric magnetic field, $\langle \boldsymbol{B} \rangle \equiv \frac{1}{2\pi L} \int_0^{2\pi} d\theta \int_0^L dz \boldsymbol{B}$, and perpendicular to it, where $\hat{\boldsymbol{e}}_\perp \equiv \hat{\boldsymbol{e}}_\parallel \times \hat{\boldsymbol{e}}_r$. This can be seen in Fig. 9. In the single-fluid MHD computation (A), the parallel kinetic energy is much larger than the perpendicular kinetic energy during and after the first event, but equipartition is observed later. In addition, the kinetic energy remains much smaller than in our two-fluid computations.

In our computations with two-fluid effects (B, C, and D), the perpendicular energy rises to many times greater than the parallel energy during a relaxation event, and this persists after the event. This large imbalance is a direct result of the two-fluid effects in the generalized Ohm's law, as the effect occurs in models with and without the ion gyroviscosity. As pointed out in Refs. 40 and 44, two-fluid effects are important in the generation of flows perpendicular to the magnetic field.

V. CONCLUSIONS

Our computations at low-β pinch parameters with $\hat{\epsilon} \ll 1$ demonstrate that the magnetic helicity is well conserved relative to magnetic energy during relaxation, in agreement with both theoretical predictions and experimental measurements on MST. This is true for single-fluid MHD and for two-fluid models with and without the ion gyroviscosity, even though the magnetic helicity alone is not an ideal invariant in our two-fluid model. The relaxation dynamics act to flatten the parallel current, and the plasma evolves towards the predicted relaxed state, although the relaxation remains incomplete.

The hybrid helicity is also well conserved relative to magnetic energy, because the hybrid helicity is dominated by the magnetic helicity at these pinch parameters relevant to magnetic confinement. In two-fluid models, differences between hybrid helicity and magnetic helicity arise at next order in $\hat{\epsilon}$, primarily from changes to the cross helicity. Two-fluid computations without ion gyroviscosity demonstrate that the two-fluid Hall term has a substantial impact on cross helicity evolution, and it tends to offset viscous effects in the numerical evolution. When ion FLR effects are included, the respective contribution to cross helicity evolution has a substantial effect in our computations. The gyroviscous contribution increases or decreases the cross helicity depending on the direction of the parallel current, and the effect is largely independent of the plasma resistivity.

Changes in parallel plasma flow are small in our single-fluid MHD computation, and there is equipartition between the parallel and perpendicular components of kinetic enery, both of which remain small relative to our two-fluid computations. Substantial changes in plasma flow are observed in our two-fluid computations, and the relaxation results in a complex flow structure. The kinetic energy in the component of flow perpendicular to the magnetic field is several times larger than the energy in the flow along the field in our computations. The magnitude of parallel flow in our two-fluid computations is comparable to experimental observations, and the magnetic energy remains much larger than the kinetic energy. Free energy from gradients in plasma flow is insignificant compared to that available from gradients in the parallel current density, and the current relaxation dynamics are much more important than the flow relaxation dynamics in magnetically confined systems.

ACKNOWLEDGMENTS

J. P. Sauppe gratefully acknowledges Drs. Vladimir Mirnov and Karsten McCollam for helpful discussions regarding reversed-field pinch dynamics and plasma relaxation. This work was supported by NSF grant PHY-0821899, and by the U.S. Department of Energy grant DE-FG02-06ER54850. This research used resources of the National Energy Research Scientific Computing Center, a DOE Office of Science User Facility supported by the Office of Science of the U.S. Department of Energy under Contract No. DE-AC02-05CH11231.

Appendix A: Time-Integrated Contributions

An estimate of the importance of each term in the evolution is found by integrating over the relaxation event. The terms in the magnetic energy evolution (Eq. (8)) integrated over each relaxation event are shown in Table II, terms in the magnetic helicity evolution (Eq. (9)) are shown in Table III, and terms in the weighted cross helicity evolution (Eq. (10)) are shown in Table IV.

Note that the sum of all terms, integrated over each event, usually differs by a small amount from the actual change in the quantity over that event. This is due to errors in the numerical temporal integration. Convergence in our computations is judged, in part, from the relative significance of the numerical divergence cleaning effects compared to the physical terms in the evolution.

Appendix B: Spatial Resolution

Our computations A, B, and C were initially performed at lower spatial resolution. The results presented in the main text utilize a polynomial of degree 5 in each finite element, and these will be referred to as the high resolution (HR) cases. Results at polynomial degree 3 are briefly discussed here, and they are referred to as the low resolution (LR) cases. The divergence cleaning coefficient, κ, is a factor of 10 larger in the LR computations than the HR computations. All other parameters are identical.

The magnetic and hybrid helicity are well conserved relative to the magnetic energy in our LR computations, and the magnitudes of the changes are similar to the HR computations. However, the numerical divergence cleaning accounts for a more significant fraction of the total magnetic energy and helicity losses. Numerical effects on magnetic

energy evolution are about $2-2.5$ times larger in the LR computations than in the HR computations, and the effects on magnetic helicity evolution are between 10 and 20 times larger than in the HR computations.

The cross helicity evolution is also similar between our LR and HR computations; $2\frac{m_i}{e}\mathcal{X}(t)/\mathcal{K}(0)$ is negative following relaxation in our LR case B, and it is positive in our LR case C, and the values of cross helicity are also comparable. There are also large changes in cross helicity in our LR case A, but this is attributed to the numerical divergence cleaning. The importance of individual terms in the evolution differs substantially in our LR cases B and C. The divergence cleaning artifact is substantial in our LR cases B and C, but it is nearly balanced by the two-fluid Hall term, which is increased commensurately and differs greatly from the HR cases B and C. Ion FLR effects still determine the direction of cross helicity evolution in our LR case C. The imbalance in axisymmetric kinetic energy in flow aligned with the magnetic field and perpendicular to it is also observed at lower resolution. In summary, all main points of Sec. IV are also evident in the LR computations, except for cross helicity evolution being driven by the Hall term in our LR case B.

[1]L. Woltjer, Proceedings of the National Academy of Sciences **44**, 489 (1958).
[2]J. B. Taylor, Physical Review Letters **33**, 1139 (1974).
[3]J. M. Finn and T. J. Antonsen, Physics of Fluids **26**, 3540 (1983).
[4]E. Hameiri, Physics of Plasmas **21** (2014).
[5]L. Turner, IEEE Transactions on Plasma Science **PS-14**, 849 (1986).
[6]L. C. Steinhauer and A. Ishida, Physical Review Letters **79**, 3423 (1997).
[7]C. C. Hegna, Physics of Plasmas **5**, 2257 (1998).
[8]S. M. Mahajan and Z. Yoshida, Physical Review Letters **81**, 4863 (1998).
[9]L. C. Steinhauer and A. Ishida, Physics of Plasmas **5**, 2609 (1998).
[10]H. K. Moffatt, Journal of Fluid Mechanics **35**, 117 (1969).
[11]A. Reiman, Physics of Fluids **24**, 956 (1981).
[12]J. M. Finn and T. J. Antonsen, Comments on Plasma Physics and Controlled Fusion **9**, 111 (1985).
[13]J. B. Taylor, Reviews of Modern Physics **58**, 741 (1986).
[14]H. A. B. Bodin and A. A. Newton, Nuclear Fusion **20**, 1255 (1980).
[15]D. J. Den Hartog, A. F. Almagri, J. T. Chapman, H. Ji, S. C. Prager, J. S. Sarff, R. J. Fonck, and C. C. Hegna, Physics of Plasmas **2**, 2281 (1995).
[16]A. Kuritsyn, G. Fiksel, A. F. Almagri, D. L. Brower, W. X. Ding, M. C. Miller, V. V. Mirnov, S. C. Prager, and J. S. Sarff, Physics of Plasmas **16**, 055903 (2009).
[17]K. Chiyoda, Journal of the Physical Society of Japan **55**, 1139 (1986).
[18]J. Shiraishi, S. Ohsaki, and Z. Yoshida, Journal of Plasma Fusion Research 6, 169 (2004).
[19]R. Horiuchi and T. Sato, Physics of Fluids **31**, 1142 (1988).
[20]D. Biskamp, E. Schwarz, and J. F. Drake, Physics of Plasmas **4**, 1002 (1997).
[21]V. V. Mirnov, C. C. Hegna, and S. C. Prager, Plasma Physics Reports **29**, 566 (2003).
[22]P. A. Cassak, J. F. Drake, M. A. Shay, and B. Eckhardt, Physical Review Letters **98**, 215001 (2007).
[23]J. R. King, C. R. Sovinec, and V. V. Mirnov, Physics of Plasmas **19**, 055905 (2012).
[24]R. Numata, Z. Yoshida, and T. Hayashi, Journal of Plasma Fusion Research 6 (2004).
[25]S. You, Physics of Plasmas **19**, 092107 (2012).
[26]Z. Yoshida and S. M. Mahajan, Physical Review Letters **88**, 095001 (2002).
[27]S. Ohsaki and Z. Yoshida, Physics of Plasmas **12** (2005).
[28]I. V. Khalzov, F. Ebrahimi, D. D. Schnack, and V. V. Mirnov, Physics of Plasmas **19** (2012).
[29]S. Ortolani and D. D. Schnack, *MHD of Plasma Relaxation* (Singapore, World Scientific, 1993).
[30]R. N. Dexter, D. W. Kerst, T. W. Lovell, S. C. Prager, and J. C. Sprott, Fusion Technology **19**, 131 (1991).
[31]H. Ji, S. C. Prager, and J. S. Sarff, Physical Review Letters **74**, 2945 (1995).
[32]C. R. Sovinec, A. H. Glasser, T. A. Gianakon, D. C. Barnes, R. A. Nebel, S. E. Kruger, D. D. Schnack, S. J. Plimpton, A. Tarditi, M. S. Chu, and the NIMROD Team, Journal of Computational Physics **195**, 355 (2004).
[33]C. R. Sovinec, J. R. King, and the NIMROD Team, Journal of Computational Physics **229**, 5803 (2010).
[34]W. X. Ding, D. L. Brower, A. F. Almagri, D. Craig, G. Fiksel, V. Mirnov, S. C. Prager, J. S. Sarff, and V. Svidzinski, Physics of Plasmas **13**, 112306 (2006).
[35]J. F. Drake and Y. C. Lee, Physics of Fluids **20**, 1341 (1977).
[36]S. I. Braginskii, Reviews of Plasma Physics **1**, 205 (1965).
[37]A. N. Kaufman, Physics of Fluids **3** (1960).
[38]D. C. Robinson, Plasma Physics **13**, 439 (1971).
[39]K. Kimura and P. J. Morrison, Physics of Plasmas **21**, 082101 (2014).
[40]J. R. King, C. R. Sovinec, and V. V. Mirnov, Physics of Plasmas **18**, 042303 (2011).
[41]A. Reiman, Physics of Fluids **23**, 230 (1980).
[42]D. L. Brower, W. X. Ding, S. D. Terry, J. K. Anderson, T. M. Biewer, B. E. Chapman, D. Craig, C. B. Forest, S. C. Prager, and J. S. Sarff, Physical Review Letters **88**, 185005 (2002).
[43]S. D. Terry, D. L. Brower, W. X. Ding, J. K. Anderson, T. M. Biewer, B. E. Chapman, D. Craig, C. B. Forest, R. O'Connell, S. C. Prager, and J. S. Sarff, Physics of Plasmas **11**, 1079 (2004).
[44]R. Numata, Z. Yoshida, and T. Hayashi, Computer Physics Communications **164**, 291 (2004).

TABLE II. Net change in magnetic energy over each relaxation event.

$\frac{1}{W_B(0)}\int dt\int d^3x$	**A** Event 1	**A** Event 2	**A** Event 3	**C** Event 1	**D** Event 1
$-\boldsymbol{\nabla}\cdot\left(\frac{\boldsymbol{E}\times\boldsymbol{B}}{\mu_0}\right)$	36.205%	27.465%	30.563%	32.289%	9.443%
$-\eta J^2$	−36.228%	−27.732%	−30.801%	−33.028%	−9.804%
$\boldsymbol{v}\times\boldsymbol{B}\cdot\boldsymbol{J}$	−1.400%	−1.095%	−1.203%	−0.837%	−0.681%
$\frac{\boldsymbol{J}}{ne}\cdot\boldsymbol{\nabla}p_e$				−0.032%	0.012%
$-\kappa\left(\boldsymbol{\nabla}\cdot\boldsymbol{B}\right)^2$	−0.052%	−0.038%	−0.039%	−0.214%	−0.724%
$-\frac{m_e}{ne^2}\frac{\partial\boldsymbol{J}}{\partial t}\cdot\boldsymbol{J}$				0.004%	0.004%
Sum	−1.475%	−1.399%	−1.482%	−1.818%	−1.749%
$\Delta W_B/W_B\,(0)$	−1.393%	−1.337%	−1.408%	−1.697%	−1.660%

$\frac{1}{W_B(0)}\int dt\int d^3x$	**B** Event 1	**B** Event 2	**B** Event 3	**B** Event 4	**B** Event 5
$-\boldsymbol{\nabla}\cdot\left(\frac{\boldsymbol{E}\times\boldsymbol{B}}{\mu_0}\right)$	30.122%	21.418%	23.056%	21.997%	22.131%
$-\eta J^2$	−30.791%	−22.086%	−24.244%	−22.980%	−22.821%
$\boldsymbol{v}\times\boldsymbol{B}\cdot\boldsymbol{J}$	−1.030%	−0.092%	−0.149%	0.042%	0.177%
$\frac{\boldsymbol{J}}{ne}\cdot\boldsymbol{\nabla}p_e$	0.000%	0.015%	0.041%	0.053%	0.035%
$-\kappa\left(\boldsymbol{\nabla}\cdot\boldsymbol{B}\right)^2$	−0.108%	−0.040%	−0.344%	−0.029%	−0.023%
$-\frac{m_e}{ne^2}\frac{\partial\boldsymbol{J}}{\partial t}\cdot\boldsymbol{J}$	0.003%	0.000%	0.002%	0.000%	0.001%
Sum	−1.804%	−0.784%	−1.638%	−0.917%	−0.500%
$\Delta W_B/W_B\,(0)$	−1.698%	−0.734%	−1.062%	−0.888%	−0.461%

TABLE III. Net change in magnetic helicity over each relaxation event.

$\frac{2}{\mathcal{K}(0)}\int dt\int d^3x$	**A** Event 1	**A** Event 2	**A** Event 3	**C** Event 1	**D** Event 1
$\boldsymbol{\nabla}\cdot\left(\boldsymbol{A}'\times\boldsymbol{E}'\right)$	30.312%	22.866%	25.598%	27.053%	7.969%
$-\eta\boldsymbol{J}\cdot\boldsymbol{B}$	−30.109%	−22.770%	−25.429%	−26.830%	−7.805%
$\frac{\boldsymbol{B}}{ne}\cdot\boldsymbol{\nabla}p_e$				0.006%	0.003%
$\frac{\kappa}{2}\boldsymbol{A}\cdot\boldsymbol{\nabla}\left(\boldsymbol{\nabla}\cdot\boldsymbol{B}\right)$	−0.002%	−0.001%	−0.002%	−0.002%	−0.006%
$-\frac{m_e}{ne^2}\frac{\partial\boldsymbol{J}}{\partial t}\cdot\boldsymbol{B}$				0.000%	0.000%
Sum	0.201%	0.095%	0.166%	0.226%	0.161%
$\Delta\mathcal{K}/\mathcal{K}\,(0)$	0.198%	0.094%	0.165%	0.229%	0.157%

$\frac{2}{\mathcal{K}(0)}\int dt\int d^3x$	**B** Event 1	**B** Event 2	**B** Event 3	**B** Event 4	**B** Event 5
$\boldsymbol{\nabla}\cdot\left(\boldsymbol{A}'\times\boldsymbol{E}'\right)$	25.230%	18.091%	19.593%	18.776%	18.860%
$-\eta\boldsymbol{J}\cdot\boldsymbol{B}$	−25.096%	−18.107%	−19.634%	−18.853%	−18.855%
$\frac{\boldsymbol{B}}{ne}\cdot\boldsymbol{\nabla}p_e$	0.018%	0.023%	0.045%	0.050%	0.036%
$\frac{\kappa}{2}\boldsymbol{A}\cdot\boldsymbol{\nabla}\left(\boldsymbol{\nabla}\cdot\boldsymbol{B}\right)$	−0.002%	−0.001%	−0.001%	−0.001%	−0.001%
$-\frac{m_e}{ne^2}\frac{\partial\boldsymbol{J}}{\partial t}\cdot\boldsymbol{B}$	0.000%	0.000%	0.000%	0.000%	0.000%
Sum	0.148%	0.005%	0.003%	−0.028%	0.039%
$\Delta\mathcal{K}/\mathcal{K}\,(0)$	0.128%	−0.002%	−0.006%	−0.025%	0.046%

TABLE IV. Net change in cross helicity over each relaxation event.

$\frac{2}{\mathcal{K}(0)}\int dt\int d^3x$	**A** Event 1	**A** Event 2	**A** Event 3	**C** Event 1	**D** Event 1
$-\frac{1}{ne}\boldsymbol{J}\times\boldsymbol{B}\cdot\frac{m_i}{e}\boldsymbol{\omega}$				−0.023%	−0.038%
$\frac{1}{ne}\boldsymbol{\nabla}p_e\cdot\frac{m_i}{e}\boldsymbol{\omega}$				−0.009%	0.001%
$-\eta\boldsymbol{J}\cdot\frac{m_i}{e}\boldsymbol{\omega}$	−0.007%	−0.009%	−0.003%	−0.050%	−0.031%
$-\frac{1}{ne}\boldsymbol{B}\cdot\boldsymbol{\nabla}\left(p_e+p_i\right)$	0.026%	−0.005%	0.000%	−0.012%	−0.006%
$-\frac{1}{ne}\boldsymbol{B}\cdot\left(\boldsymbol{\nabla}\cdot\underline{\boldsymbol{\Pi}}_{iso}\right)$	−0.039%	−0.033%	−0.024%	0.224%	0.167%
$-\frac{1}{ne}\boldsymbol{B}\cdot\left(\boldsymbol{\nabla}\cdot\underline{\boldsymbol{\Pi}}_{gyr}\right)$				0.349%	0.395%
$\kappa\frac{m_i}{e}\boldsymbol{v}\cdot\boldsymbol{\nabla}\left(\boldsymbol{\nabla}\cdot\boldsymbol{B}\right)$	0.002%	0.003%	−0.003%	−0.022%	−0.153%
$\frac{m_e}{ne^2}\frac{\partial\boldsymbol{J}}{\partial t}\cdot\frac{m_i}{e}\boldsymbol{\omega}$				0.001%	−0.001%
Sum	−0.017%	−0.043%	−0.030%	0.458%	0.334%
$2\frac{m_i}{e}\Delta\mathcal{X}/\mathcal{K}\left(0\right)$	−0.035%	−0.026%	−0.040%	0.437%	0.310%

$\frac{2}{\mathcal{K}(0)}\int dt\int d^3x$	**B** Event 1	**B** Event 2	**B** Event 3	**B** Event 4	**B** Event 5
$-\frac{1}{ne}\boldsymbol{J}\times\boldsymbol{B}\cdot\frac{m_i}{e}\boldsymbol{\omega}$	0.079%	−0.045%	−0.242%	−0.097%	−0.136%
$\frac{1}{ne}\boldsymbol{\nabla}p_e\cdot\frac{m_i}{e}\boldsymbol{\omega}$	0.000%	0.005%	−0.025%	−0.015%	−0.016%
$-\eta\boldsymbol{J}\cdot\frac{m_i}{e}\boldsymbol{\omega}$	0.011%	0.002%	0.021%	0.026%	0.037%
$-\frac{1}{ne}\boldsymbol{B}\cdot\boldsymbol{\nabla}\left(p_e+p_i\right)$	−0.036%	−0.046%	−0.089%	−0.101%	−0.071%
$-\frac{1}{ne}\boldsymbol{B}\cdot\left(\boldsymbol{\nabla}\cdot\underline{\boldsymbol{\Pi}}_{iso}\right)$	0.160%	0.185%	0.226%	0.247%	0.234%
$-\frac{1}{ne}\boldsymbol{B}\cdot\left(\boldsymbol{\nabla}\cdot\underline{\boldsymbol{\Pi}}_{gyr}\right)$					
$\kappa\frac{m_i}{e}\boldsymbol{v}\cdot\boldsymbol{\nabla}\left(\boldsymbol{\nabla}\cdot\boldsymbol{B}\right)$	−0.239%	−0.099%	−0.063%	−0.066%	−0.061%
$\frac{m_e}{ne^2}\frac{\partial\boldsymbol{J}}{\partial t}\cdot\frac{m_i}{e}\boldsymbol{\omega}$	0.002%	0.001%	0.002%	0.001%	0.001%
Sum	−0.023%	0.003%	−0.171%	−0.003%	−0.012%
$2\frac{m_i}{e}\Delta\mathcal{X}/\mathcal{K}\left(0\right)$	0.000%	0.037%	−0.134%	−0.001%	0.030%